Zinc tin oxide thin film transistors produced by a high rate reactive sputtering: effect of tin composition and annealing temperatures

Kham M. Niang [*,1], **Junhee Cho[1], Aditya Sadhanala[2], William I. Milne[1], Richard H. Friend[2] and Andrew J. Flewitt[1]**

[1] Electrical Engineering Division, Department of Engineering, University of Cambridge, 9 JJ Thomson Avenue, Cambridge, CB3 0FA, United Kingdom

[2] Department of Physics, University of Cambridge, 19 JJ Thomson Avenue, Cambridge, CB3 0HE, United Kingdom

* Corresponding author: e-mail kmn36@cam.ac.uk, Phone: +44 (0)1223 748305, Fax: +44 (0)1223 748348

Amorphous zinc tin oxides (a-ZTO) which are stoichiometrically close to the Zn_2SnO_4 and $ZnSnO_3$ phases have been deposited using remote-plasma reactive sputtering, and are incorporated as the channel layers in thin film transistors (TFTs). The influence of tin composition and annealing temperatures on the structural and phase evolutions of the thin films and the electrical performances of the TFTs are investigated. Zn_2SnO_4 exhibited randomly oriented polycrystalline peaks at annealing temperatures ≥ 700 °C, while $ZnSnO_3$ decomposed into Zn_2SnO_4 and SnO_2 at 950 °C. TFTs employing a Zn_2SnO_4 channel, after a post-deposition annealing at 500 °C, exhibited a field effect mobility ~ 14 $cm^2V^{-1}s^{-1}$ and a sub-threshold slope ~ 0.6 V dec^{-1}. When the tin content is increased in the channel, as in $ZnSnO_3$, TFTs exhibited an increase in field effect mobility ~ 20 $cm^2V^{-1}s^{-1}$ but with a slight deterioration of sub-threshold slope to ~ 0.8 V dec^{-1}. When the post-deposition annealing temperature is reduced to 300 °C, a mobility as high as ~ 10 $cm^2V^{-1}s^{-1}$ is still achieved, however a significant shoulder in the I_{DS}-V_{GS} curve together with a higher off-state current is observed. TFT characteristics are explained by the sub-bandgap defect states measured by photothermal deflection spectroscopy and the extracted Urbach energies.

1 Introduction Ionic oxide semiconductors are important materials for large area electronic displays due to their high carrier mobility, transparency, and the possibility of processing at low temperatures. Indium gallium zinc oxide (IGZO) TFTs show carrier mobility of ~ 10 $cm^2V^{-1}s^{-1}$, which is an order of magnitude higher than that of hydrogenated amorphous silicon (a-Si:H) [1]. However, this material system is rather complex with three metal cations, two of which are expensive and resource-scarce elements. Given that a wide variety of oxides are available, research into simpler and less expensive material systems are vitally important from an economic point of view. Amorphous zinc tin oxide (a-ZTO) fits such a system and it has been previously reported that a-ZTO TFTs show high electron mobility [2]. Recent studies on a-ZTO as a replacement for indium tin oxide anodes in OLED displays [3], the buffer layer in oxide solar cells [4], and the active layer in sensors [5] have clearly demonstrated the technological importance and versatility of this material for various applications.

Most oxides are produced by r.f. magnetron sputtering from ceramic targets, but the growth rate is very modest (a few nm min^{-1}) and the films tend to be highly stressed [6]. Reactive sputtering generally has a higher deposition rate, and allows the use of metal targets which are more durable and cheaper than ceramic targets, thus lowering production costs [7]. However, reactive sputtering is not widely utilized for the development of a-ZTO TFTs; this is the motivation for this work.

In this report, a-ZTO thin films are reactively sputtered from zinc:tin alloy targets with Sn compositions of 10, 33 and 50 at.%, and an optimized oxygen flow. Preferential sputtering results in the tin composition being higher in the films than in the targets. We have first systematically investigated the crystallographic properties and stoichiometry of thin films after annealing at temperatures up to 950 °C and characterised these by X-ray diffraction (XRD) and scanning electron microscopy (SEM). Films deposited from 10 and 33 at.% targets are found to have tin compositions of 33 and 50 at.% respectively, resulting in stoichiometries of the two common crystalline phases of ZTO: inverse spinel Zn_2SnO_4 and ilmenite $ZnSnO_3$. These films have been successfully incorporated as channel layers in TFTs. Best performing TFTs consistently show field effect mobility as high as 20 $cm^2V^{-1}s^{-1}$, switching ratio of ~ 10^8 and sub-threshold slope ~ 0.7 $Vdec^{-1}$, which are obtained with a post-deposition annealing at 500 °C. TFTs incorporating a-ZTO channel layer with lower annealing temperature are also reported. The effect of tin compositions and annealing temperatures on TFT performances are explained by the measured sub-bandgap defect states and Urbach energy.

2 Experimental details a-ZTO thin films were deposited without intentional substrate heating onto various substrates from the Zn:Sn metal alloy targets with atomic tin contents of 10, 33 and 50 %. As references, ZnO and SnO_2 thin films are also sputtered from pure metal targets. The chamber pressure during sputtering was ~ 6 $\times10^{-3}$ mbar which was achieved with argon and oxygen flows of 60 sccm and 35 sccm respectively. An RF launch power of 800 W and a target bias power of 500 W were used. The details of the sputtering system can be found elsewhere [8]. A-ZTO and ZnO layers which are used for film characterisations are ~ 250 to 350 nm thick and those used for TFT channel layers are ~ 50 nm thick. Post-deposition annealing of the films was performed at temperatures between 300 and 950 °C in an oven in air. The annealing time was 1 hour, except for two samples annealed at 950 °C (ZTO50 and ZTO65) where the annealing time was reduced to 45 minutes.

The film thickness was determined using a Gaertner He–Ne (633 nm) ellipsometer and Veeco Dektak profilometer. The crystallinity of the films was determined by a Phillips PW 1820 XRD using a Cu-Kα radiation and a monochromator with the divergence slit and receiving slit setting of 0.5 mm and 0.2 mm respectively. SEM images and estimation of chemical composition were performed on a Leo Gemini 1530VP FEG SEM/EDX system. A more accurate ThermoScientific Multilab-2000 X-ray photoelectron spectroscopy was also used on some selected films. The electronic density of states within the bandgap was examined using photothermal deflection spectroscopy (PDS), which is a very sensitive optical absorption technique [9].

Bottom gate, inverted staggered structure TFTs were fabricated using thermally-grown SiO_2 films of 200 nm thickness as the gate dielectric and heavily-doped p-type Si (100) substrates as the gate electrode. Thermally evaporated aluminium (~ 270 nm) was used as the source and drain contacts. The active layer and the source/drain contacts were deposited and patterned using conventional photolithography and lift off methods after annealing. The TFTs with channel width to lengh ratio of 50 (W/L = 1000 μm / 20 μm) were measured in the dark, at room temperature using a Wentworth probe station inside a Faraday cage with a HP4140B dual voltage source picoammeter.

3 Results and Discussion

3.1 Thin film characterisations Figure 1 shows the deposition rate as a function of tin composition in the films (Sn/(Zn+Sn) in atomic %). The deposition rate is the lowest for pure ZnO (~ 12 nm min^{-1}) and is the highest for pure SnO_x (~ 34 nm min^{-1}). The deposition rate of ZTO varies between 15 to 22 nm min^{-1} and it increases monotonically with the tin composition in the film.
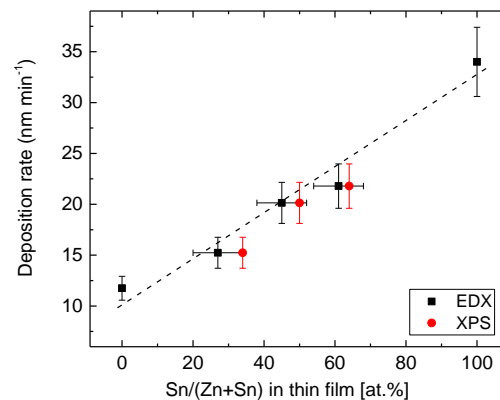

Figure 1 Deposition rate as a function of tin in the ZTO thin films. A dashed line is drawn as a guide to the eye.

The tin composition in ZTO is determined by EDX on most of the films and by XPS on selected films. It is found that the ZTO film which was sputtered from a zinc:tin alloy target with 10% Sn actually contains ~ 33% Sn. Similarly, ZTO films sputtered from a zinc:tin alloy target with 33% and 50% Sn contain ~ 50% and ~ 65% Sn respectively. Referring to the more accurate XPS data in Figure 1, the increase of tin in the films compared with the target is found to be a factor of 1.3 to 3.3. This is due to preferential sputtering which is commonly encountered in sputtering from a target with two or more elements [10]. It is also observed in rf magnetron sputtering but to a lesser degree, by a factor of 1.3 only [11-13]. In reactive sputtering, accurate flow of oxygen would be necessary to produce an oxide

with the correct stoichiometry. Moreover, the deposition rate is also generally higher when sputtering from a metal target than a ceramic target. Therefore, it is not surprising that preferential sputtering is more pronounced in reactive sputtering from a metal than in magnetron sputtering from a ceramic.

From here on, the ZTO films will be referred to as ZTO33, ZTO50 and ZTO65 according to their tin composition in the film determined by XPS. The stoichiometry of the ZTO33 and ZTO50 are very close to the stoichiometry of Zn_2SnO_4 and $ZnSnO_3$ respectively, which are the two common ZTO crystals.

Figure 2 shows the X-ray diffractogram of ZTO33, ZTO50 and ZTO65 films as-deposited and after annealing at various temperatures. As shown in Figure 2a, the as-deposited ZTO33 show diffraction peaks relating to those of the silicon substrate only, thus indicating that the film is likely to be amorphous. The film still appears to be amorphous after annealing at 500 °C. Small peaks appear at $2\theta = 17.9, 29.3, 34.6$ and 42.1 ° after annealing at 700 °C and their intensities increase after annealing at 900 °C, along with the appearance of new smaller peaks at 36.1, 44.5, 52.1 and 60.4 °. These peaks match exactly with the power diffraction patterns of Zn_2SnO_4. Therefore, it is confirmed that ZTO33 deposited by reactive sputtering is indeed stoichiometrically Zn_2SnO_4.

Our results are consistent with previously reported Zn_2SnO_4 using rf magnetron sputtering from ceramic targets, and are also very similar to the temperature range at which recrystalliztion begins. Randomly oriented polycrystalline structured Zn_2SnO_4 has been reported at 660 °C by Young et al. [12], and at 750 °C by Satoh et al. [11]. Interestingly films with (111) only orientation are also reported in the latter paper when sputtering with oxygen and argon gas mixtures [11]. When spray pyrolysis was used, a thermal treatment in air at 1000 °C up to 10 hours is needed to obtain the polycrystalline Zn_2SnO_4 phase [14].

As shown in Figure 2b, the ZTO50 film is amorphous both as-deposited and after annealing at 500 °C, similar to ZTO33 in Figure 2a. However, unlike ZTO33, the ZTO50 film still remains amorphous even after annealing at 700 °C. After annealing at 950 °C, diffraction peaks relating to Zn_2SnO_4 appear. Additionally, new peaks at $2\theta = 26.8, 38.1$ and 52 ° also appear. These new peaks match the (110), (200) and (211) peaks of SnO_2. Based on its stoichiometry, the ZTO50 should have exhibited peaks relating to $ZnSnO_3$ after annealing, but that is not the case. Instead, peaks that are related to both Zn_2SnO_4 and SnO_2 are observed. It has been previously reported that the $ZnSnO_3$ is decomposed into Zn_2SnO_4 and SnO_2 at temperatures between 700 to 800 °C [15]. That is in the same temperature range when ZTO50 recrystallizes and changes phase. It is also noted that the intensity of SnO_2 peaks are higher than the Zn_2SnO_4 peak.
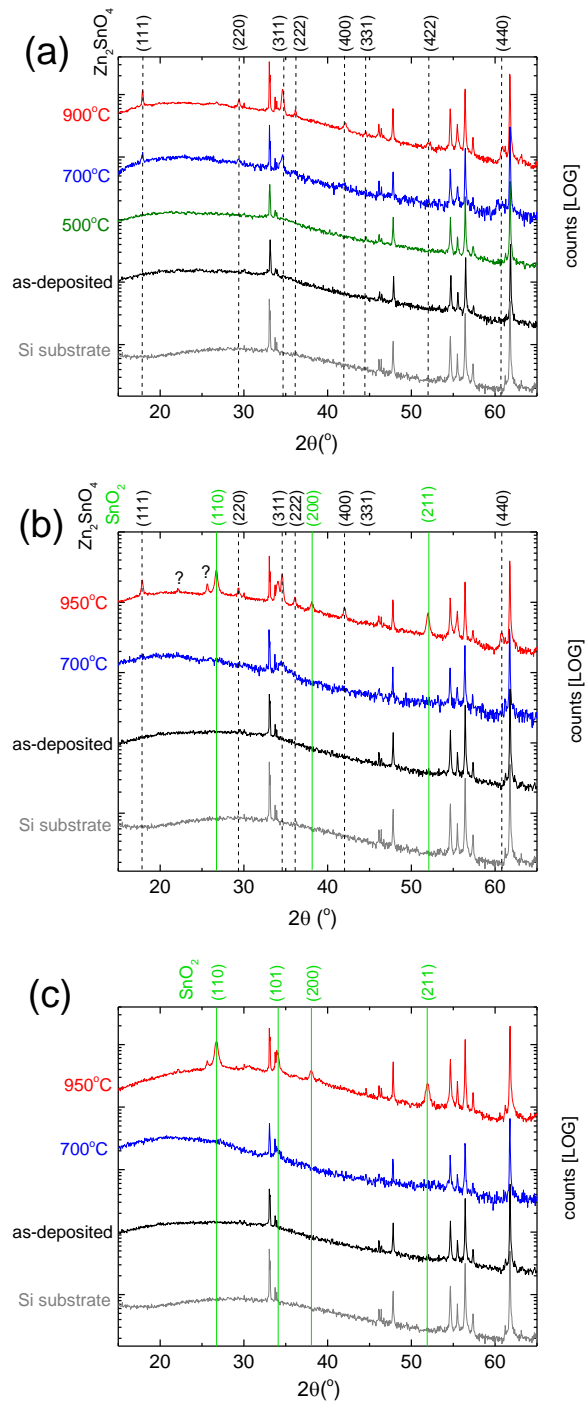

Figure 2 X-ray diffractogram of ZTO33, ZTO50 and ZTO65 (a-c) films as-deposited and after annealing at various temperatures. XRD of silicon is also shown to highlight substrate related peaks. (?) indicates peaks which are unidentified. Diffraction peaks of Zn_2SnO_4 (JCPDF 24–1470) are shown as dashed lines and those of SnO_2 (JCPDF 44–1445) are shown as solid lines.

Finally, XRD scans for ZTO65 are shown in Figure 2c. Similar to ZTO50 in Figure 2b, the ZTO65 remains amorphous after annealing up to 700 °C. After annealing at 950 °C, only peaks relating to SnO_2 appear but none relating to Zn_2SnO_4. It is also noteworthy that the intensities of the SnO_2 peaks are equally as high in ZTO65 as in ZTO50. At this point, ZTO65 looks very similar to pure SnO_2 sputtered using dc magnetron sputtering at 250 °C [16] or that produced by plasma enhanced chemical vapor deposition at 250 °C [17]. The chemical compositions of ZTO65 was not checked on this annealed sample, but it is very likely that zinc ablation has occurred [18]. In fact, when zinc stannate was prepared by spray pyrolysis, precursors with a zinc:tin ratio of 4:1 were needed to account for the loss by evaporation of zinc oxide during a very long heat treatment at 1000 °C [14].

SEM is used to investigate the surface morphology of ZTO films after annealing at temperatures $\geq$ 700 °C. In Figure 3a, the top view SEM micrograph of ZTO33 after annealing at 700 °C shows a smooth surface with small but distinctive round grains. The SEM image after 500 °C (not shown) shows a similarly smooth surface, but with fewer round grains. Since XRD in Figure 2a indicates a predominantly amorphous film at 500 °C and small polycrystalline peaks at 700 °C, the round grains indicate some local, short range ordering of crystals. After annealing at 900 °C (Figure 3b), the ZTO33 film shows irregular grains with large variation in sizes between 50 to 600 nm. This is reflected in the higher intensity of the XRD peaks (Figure 2a). It is difficult to compare the microstructures of Zn_2SnO_4 between samples which were prepared by different methods, nonetheless SEM images of relatively homogenous, irregularly shaped grains or agglomerates have been reported by various groups [14,19].

SEM images of the film with highest tin composition, ZTO65 in Figure 3e-f is discussed next. After annealing at 700 °C, ZTO65 shows a smooth homogenous surface. This agrees well with the amorphous phase seen in XRD in Figure 2c. After annealing at 950 °C, ZTO65 shows a uniform surface with densely packed grains. The inset of Figure 3f shows multi-facetted grains which vary in size between 20 to 100 nm. Combining with the XRD data, these are shown to be SnO_2 grains in random orientations. Recently, Ji *et al.*, who deposited SnO_2 using rf magnetron sputtering at 700 °C from a ceramic target under oxygen partial pressures between 0 to 20%, demonstrated how the crystal orientation and grain structure change even with a small change in oxygen partial pressure [20]. The SEM image and XRD pattern of their polycrystalline SnO_2 sputtered with oxygen partial pressure of 5 % are found to be remarkably similar to those of our ZTO65 film annealed at 950 °C.

Finally, the ZTO50 sample is examined. As shown in Figure 3c, it shows a smooth homogenous surface after annealing at 700 °C, and appears amorphous as also confirmed by XRD. At this stage, ZTO50 and ZTO65 look very similar. After annealing at 950 °C, a rough uneven surface appears. The zoom-out SEM image (not shown) shows a bubble-like surface (sizes ~ 2 to 20 μm) and a few of them are already ruptured producing flakes. According to XRD, ZTO50 is composed of two phases, Zn_2SnO_4 and SnO_2. Moreover, the intensities are higher in peaks relating to SnO_2 than Zn_2SnO_4, which could be interpreted as the SnO_2 dominating. However, the surface microstructures show no resemblance to either SnO_2 or Zn_2SnO_4. This requires further investigation.
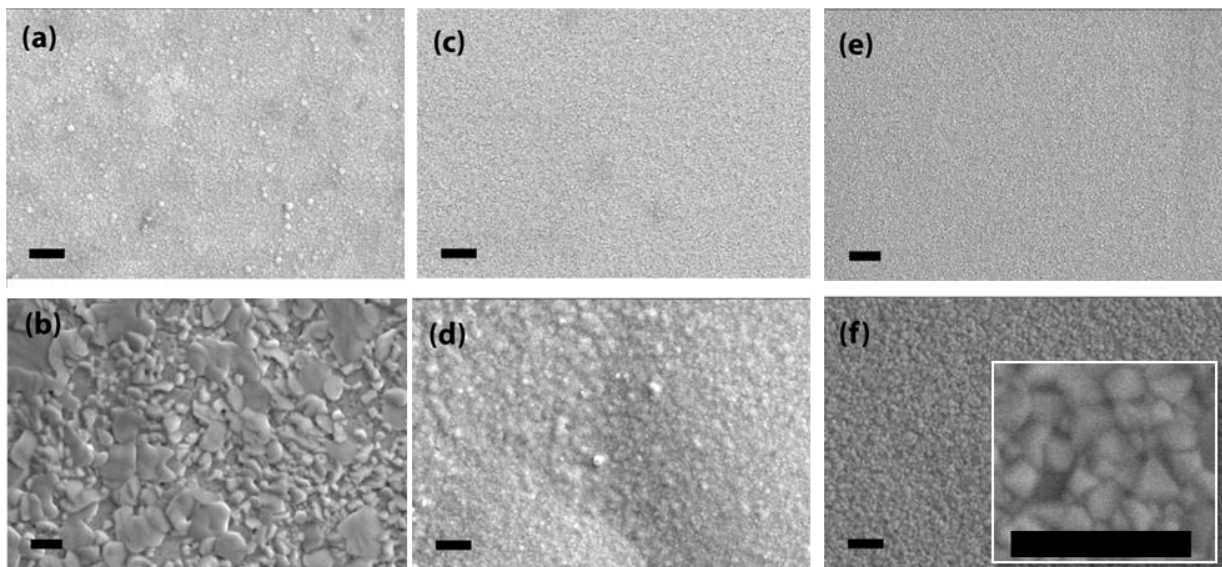

Figure 3 Top view scanning electron micrographs of ZTO thin films. In the top row are the ZTO33, ZTO50 and ZTO65 after annealing at 700 °C (a, c, and e). In the bottom row are the ZTO33 after annealing at 900 °C (b), ZTO50 and ZTO65 after annealing at 950 °C (d and f) respectively. Inset of figure 3f is a zoom-in of the grains. The scale bars are 400 nm.

It should be noted that the ZTO33 and ZTO50 films that are used as the channel layer in TFTs are annealed at temperatures ≤ 500 °C, thus they would be still amorphous. They may look very similar having smooth, highly uniform surfaces, but they are very different materials and are stoichiometrically very close to Zn_2SnO_4 and $ZnSnO_3$ respectively.

3.2 Thin film transistors

3.2.1 Effect of tin compositions Figure 4 shows an overlay of the gate transfer characteristics for the ZnO, ZTO33, ZTO50 and ZTO65 TFTs. The field effect mobility, μ_{FE}, is calculated from,

$$\mu_{FE} = \frac{\left[\partial I_{DS} / \partial V_{GS}\right]}{C_{ox}\left(W/L\right)V_{DS}} \qquad (1)$$

where $\partial I_{DS} / \partial V_{GS}$ is the transconductance, C_{ox} is the oxide capacitance, and W/L is the width to length ratio of the channel. The ZnO TFT exhibited a μ_{FE} of 0.7 cm^{2}V^{-1}s^{-1}, a sub-threshold slope ~ 4 Vdec^{-1} and a switching ratio of 10^6. A significant improvement in performance is observed in the ZTO33 TFT, exhibiting μ_{FE} of 13.5 cm^{2}V^{-1}s^{-1}, a threshold voltage ~ 10 V, sub-threshold slope ~ 0.55 V dec^{-1} and switching ratio of 5×10^8. A further increase in μ_{FE} (20.2 cm^{2}V^{-1}s^{-1}) is observed in ZTO50 with threshold voltage ~ 8.3 V, sub-threshold slope ~ 0.78 V dec^{-1} and a switching ratio of 5×10^8. It is noteworthy that the hysteresis is very small in our devices. Finally, the ZTO65 TFT exhibited no transistor characteristics and it could no long-

er be used as a semiconductor channel. The TFT parameters are summarised in Table 1.

It is well established that the performance of ZnO TFTs is greatly limited by the grain boundaries of the polycrystalline ZnO channel [21].

In Figure 4, a sharp increase of field effect mobility in ZnO to ZTO33, and a further increase to ZTO50 can be attributed to (i) the lack of grain boundaries in the channel layer arising from the amorphous nature of multicomponent oxides, and (ii) the effect of metal cation incorporation, as in this case, tin with its valency (+2 or +4) will contribute more free carriers [1]. Another advantage of incorporation of heavy metal cations is the suppression of oxygen vacancy formation, which is attributed to their higher bond strength over ZnO. Suppression of oxygen vacancies then enables a very low off state current [22]. Such a scheme has been employed in material systems other than zinc oxide; in this case, silicon dioxide is incorporated into indium oxide based TFTs [23].

However, the increase in carrier concentration and thus mobility in ZTO50 comes at the expense of higher sub-threshold slope as it is increased from 0.55 to 0.78 V dec^{-1}. As the carrier concentration is further increased to ~ 65% as shown in ZTO65, channel depletion can no longer be achieved.

It is well established that TFT performances are strongly affected by defect tail states and sub-bandgap states originating from structural disorder and defects [24]. These states are measured by PDS which is widely utilized in various applications [25,26]. Figure 5 shows the absorption spectra as a function of sub-bandgap energies (≤ 3.2 eV) for the three ZTO films annealed at 500 °C, which is the same anneal temperature as for the channel layers.
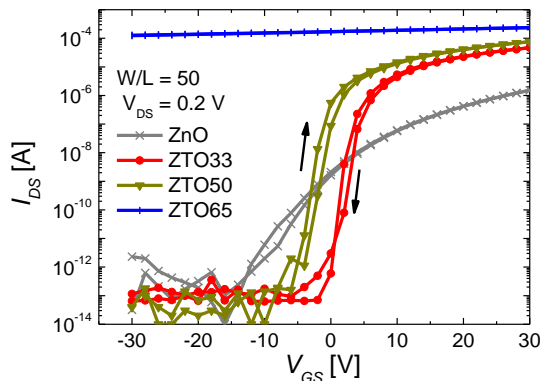
Figure 4 Gate transfer characteristics for the ZTO and ZnO TFTs measured with V_{DS} = 0.2 V. A post-deposition annealing of the channel layer is performed at 500 °C for 1 hour in air.
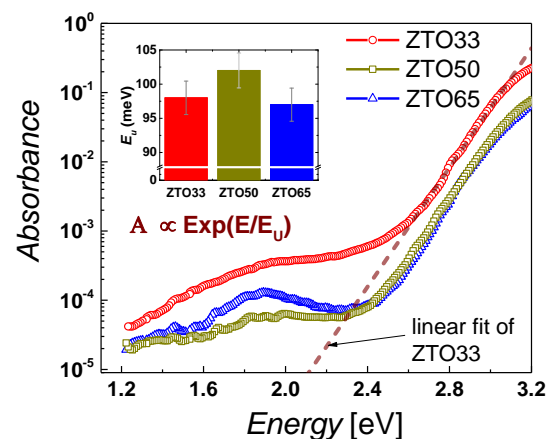
Figure 5 Absorption spectra for ZTO thin films annealed at 500 °C obtained using PDS. Inset shows the corresponding Urbach energy extracted by fitting the band-tail.
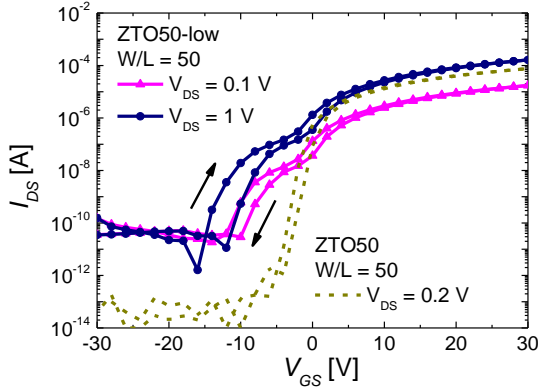
Figure 6 Gate transfer characteristics for the ZTO50-low TFTs measured with V_{DS} = 0.1 and 1 V. The channel layer is annealed at 300 °C for 1 hour in air. For comparison the ZTO50 TFT is also shown.
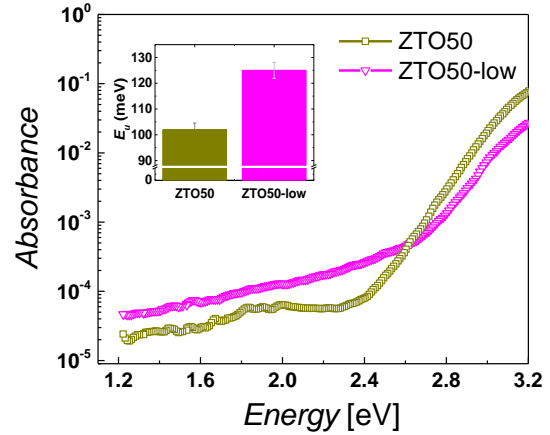

Figure 7 PDS absorption spectra for ZTO thin films annealed at either 300 °C (ZTO50-low) or 500 °C (ZTO50). Inset shows the corresponding Urbach energy extracted by fitting the band-tail.

The extracted Urbach energy, E_U, for ZTO33, ZTO50 and ZT65 are very similar: 98, 102 and 97 meV respectively. These values are lower than the previously reported Urbach energies for ZTO (110 meV) and IGZO (110 ~ 160 meV) [22,27,28]. A very low Urbach energy ~ 22 meV has also been reported for IGZO [29]. It should be noted that different measurement techniques were used in all these papers. Since lower Urbach energy means fewer defect states in the bandgap, we can say that our ZTO films are of very good quality, which is also indicated by the device performance. It is generally accepted that the defect states detected by PDS are dominated by those at the valence band edge [27], which agrees well with the ZTO65 result in that it is not switching off because of excess carriers in the conduction band tails and not because of higher defects in the valence band tails.

Also shown in Figure 5 is the absorbance deep in the sub-bandgap (1.2 eV < E < 2.2 eV) and it is the highest in ZTO33, followed by ZTO65 and then ZTO50. The differences in the absorbance levels between samples are large, but there is no strong correlation observed between absorbance (deep defect states) and tin concentrations in a-ZTO.

3.2.2 Effect of annealing temperatures TFTs are fabricated employing ZTO50 with a lower post-deposition annealing at 300 °C (denoted as ZTO50-low) as shown in Figure 6. With a 300 °C anneal, TFT characteristics are observed but with a higher off-state current, I_{OFF} ~ 10^{-10} A and a significant shoulder around V_{GS} = 0 V. Compare to ZTO50 which is turned on at V_{GS} ~ –5 V, the ZTO50-low turned on at V_{GS} ~ –15 V. The device turn-on voltage is also sensitive to the applied V_{DS}. In the accumulation region, an order of magnitude increase in the I_{DS} is observed as V_{DS} is increased from 0.1 to 1 V. Despite being less than ideal

devices, a high μ_{FE} ~ 10 cm^{2}V^{-1}s^{-1} is still achieved in ZTO50-low TFTs. Device parameters are also summarised in Table 1.

Table 1 Transistor parameters of ZnO and ZTO TFTs with a channel W/L ratio of 50, measured with a V_{DS} of 0.1 or 0.2 V (as shown in Figure. 4 and 6).

TFTs	V_{th} [V]	μ_{FE} [cm^{2}V^{-1}s^{-1}]	S.S [Vdec^{-1}]	I_{ON}/I_{OFF}
ZnO	17.6	0.7	4.0	10^6
ZTO33	10.0	13.5	0.55	5 × 10^8
ZTO50	8.3	20.2	0.78	5 × 10^8
ZTO50-low	9.6	9.8	2.5	5 × 10^5

From the PDS absorption spectra in Figure 7, the Urbach energy for ZTO50-low is extracted to be 125 meV, which is a significant increase from the 102 meV of ZTO50. This indicates that the density of defect states is higher with lower annealing temperatures. Therefore, there is a strong correlation between ZTO annealing temperatures and the Urbach energy. Moreover, the absorbance deep in the sub-bandgap is also higher in ZTO50-low than ZTO50, again showing strong correlation between ZTO annealing temperatures and deep defect states.

From our TFT and PDS data (Figures 4 to 7), it is observed that the effect of annealing temperatures on the ZTO TFT performance can be examined by the measured density of sub-bandgap states. This is consistent with a previous report on the use of PDS for organic devices [30]. On the other hand, the effect of tin compositions on the ZTO TFT performance does not show a strong correlation. However, the Urbach energy extracted is still valuable to gauge the quality of the semiconductors.

Finally, the XRD and SEM analysis show that the ZTO33 and ZTO50 are very different crystalline structures and are also at different stages of crystallinity at a given annealing temperature. It can also be postulated that they will have different local short range order in their amorphous phases. This difference, which arises from different tin composition in the films, is in turn possibly related to the different field effect mobility obtained for the ZTO33 and ZTO50 TFTs. It is shown here that reactive sputtering achieves good devices from films with large window of zinc-to-tin ratio. This is consistent with wide process window of ZTO TFTs produced by other methods such as rf magnetron sputtering, pulse laser deposition and chemical vapour deposition [31-33]. One drawback of the reactive sputtering is the preferential sputtering of one metal over another, which would shorten the lifetime of such a target in a production environment.

4 Conclusions a-ZTO thin films have been deposited using remote-plasma reactive sputtering from zinc:tin alloy targets with various tin compositions. Optimised films are found to be stoichiometrically close to the common Zn_2SnO_4 and $ZnSnO_3$ phases, which is confirmed by XRD and SEM on films annealed at various temperatures. At annealing temperatures ~ 900 °C, the Zn_2SnO_4 still remains stable but $ZnSnO_3$ is decomposed to Zn_2SnO_4 and SnO_2. TFTs incorporating these materials, after a post-deposition annealing at 500 °C, exhibited good electrical characteristics with field effect mobilities ~ 14 to 20 $cm^2V^{-1}s^{-1}$. The field effect mobility increases with tin compositions but the Urbach energy does not vary with tin composition. On the other hand, the Urbach energy increases when the annealing temperature is reduced from 500 to 300 °C, indicating that the defects in the bandgap increase. A field effect mobility ~ 10 $cm^2V^{-1}s^{-1}$ is still obtained in devices with 300 °C annealed ZTO, but there is a large shoulder at V_{GS} ~ 0V in the I_{DS}-V_{GS} curve. The Urbach energies of the a-ZTO in this work are slightly lower than those previously reported for a-ZTO and a-IGZO. In summary it is shown that a-ZTO with very different tin compositions and microstructures are able to produce highly performing TFTs with mobilities in the same order.

References

[1]   K. Nomura, H. Ohta, A. Takagi, T. Kamiya, M. Hirano, and H. Hosono, Nature **432**, 488 (2004).

[2]   H. Q. Chiang, J. F. Wager, R. L. Hoffman, J. Jeong, and D. A. Keszler, Appl. Phys. Lett. **86**, 013503 (2005).

[3]   M. Morales-Masis *et al.*, Adv. Funct. Mater. **26**, 384 (2016).

[4]   Y. S. Lee, J. Heo, S. C. Siah, J. P. Mailoa, R. E. Brandt, S. B. Kim, R. G. Gordon, and T. Buonassisi, Energy Environ. Sci **6**, 2112 (2013).

[5]   S. Dutta and A. Dodabalapur, Sens. Actuators B **143**, 50 (2009).

[6]   J. A. Thornton and D. W. Hoffman, J. Vac. Sci. Technol. **14**, 164 (1977).

[7]   D. Hong, H. Q. Chiang, and J. F. Wager, J. Vac. Sci. Technol. B **24**, L23 (2006).

[8]   S. J. Wakeham, M. J. Thwaites, B. W. Holton, C. Tsakonas, W. M. Cranton, D. C. Koutsogeorgis, and R. Ranson, Thin Solid Films **518**, 1355 (2009).

[9]   W. B. Jackson and N. M. Amer, Phys. Rev. B **25**, 25 (1982).

[10]   R. Kelly and D. E. Harrison, Mater. Sci. Eng. **69**, 449 (1985).

[11]   K. Satoh, Y. Kakehi, A. Okamoto, S. Murakami, F. Uratani, and T. Yotsuya, Jpn. J. Appl. Phys. **44**, L34 (2005).

[12]   D. L. Young, H. Moutinho, Y. Yan, and T. J. Coutts, J. Appl. Phys. **92**, 310 (2002).

[13]   J. S. Rajachidambaram, S. Sanghavi, P. Nachimuthu, V. Shutthanandan, T. Varga, B. Flynn, S. Thevuthasan, and G. S. Herman, J. Mater. Res., **27**, 2309 (2012).

[14]   I. Stambolova, K. Konstantinov, D. Kovacheva, P. Peshev, and T. Donchev, J. Solid State Chemistry **128**, 305 (1997).

[15]   Y.-S. Shen and T.-S. Zhang, Sens. Actuators B **12**, 5 (1993).

[16]   Y. Hayashi, K. Kondo, K. Murai, T. Moriga, I. Nakabayashi, H. Fukumoto, and K. Tominaga, Vacuum **74**, 607 (2004).

[17]   J. J. Robbins, Y.-J. Huang, M. Bai, T. L. Vincent, and C. A. Wolden, Mat. Res. Soc. Symp. Proc. **666**, F1.7.1 (2001).

[18]   C. Tsakonas, W. Cranton, F. Li, K. Abusabee, A. Flewitt, D. Koutsogeorgis, and R. Ranson, Journal of Physics D: Applied Physics **46**, 095305 (2013).

[19]   N. Nikolic, T. Sreckovic, and M. M. Ristic, Journal of the European Ceramic Society **21**, 2071 (2001).

[20]   Y.-C. Ji, H.-X. Zhang, X.-H. Zhang, and Z.-Q. Li, Physica status solidi (b) **250**, 2145 (2013).

[21]   A. J. Flewitt *et al.*, Semicond. Sci. Technol. **24**, 085002 (2009).

[22]   T. Kamiya and H. Hosono, NPG Asia Materials **2**, 15 (2010).

[23]   N. Mitoma, S. Aikawa, X. Gao, T. Kizu, M. Shimizu, M.-F. Lin, T. Nabatame, and K. Tsukagoshi, Appl. Phys. Lett. **104**, 102103 (2014).

[24]   J. Robertson, Journal of Non-Crystalline Solids **358**, 2437 (2012).

[25]   A. Sadhanala *et al.*, J Phys Chem Lett **5**, 2501 (2014).

[26]   R. L. Hoye, S. Heffernan, Y. Ievskaya, A. Sadhanala, A. Flewitt, R. H. Friend, J. L. MacManus-Driscoll, and K. P. Musselman, ACS applied materials & interfaces **6**, 22192 (2014).
[27]   P. T. Erslev, E. S. Sundholm, R. E. Presley, D. Hong, J. F. Wager, and J. D. Cohen, Applied Physics Letters **95**, 192115 (2009).
[28]   E. K.-H. Yu, S. Jun, D. H. Kim, and J. Kanicki, Journal of Applied Physics **116**, 154505 (2014).
[29]   K. Nomura, T. Kamiya, H. Yanagi, E. Ikenaga, K. Yang, K. Kobayashi, M. Hirano, and H. Hosono, Applied Physics Letters **92**, 202117 (2008).
[30]   J. Socratous, K. K. Banger, Y. Vaynzof, A. Sadhanala, A. D. Brown, A. Sepe, U. Steiner, and H. Sirringhaus, Adv Funct Mater **25**, 1873 (2015).
[31]   R. L. Hoffman, Solid-State Electronics **50**, 784 (2006).
[32]   P. Görrn, P. Hölzer, T. Riedl, W. Kowalsky, J. Wang, T. Weimann, P. Hinze, and S. Kipp, Appl. Phys. Lett. **90**, 063502 (2007).
[33]   U. K. Kim *et al.*, J. Mater. Chem. C **1**, 6695 (2013).